



# An $hp$ -adaptive discontinuous Galerkin method for modelling snap loads in mooring cables



Johannes Palm<sup>\*</sup>, Claes Eskilsson<sup>1</sup>, Lars Bergdahl

Department of Mechanics and Maritime Sciences, Chalmers University of Technology, SE-412 96, Gothenburg, Sweden

## ARTICLE INFO

### Keywords:

Mooring cable  
Snap load  
Discontinuous Galerkin method  
High-order  
Shock-capturing

## ABSTRACT

This paper focuses on modelling snap loads in mooring cables. Snap loads are a known problem for the established oil and gas industry, and they pose a major challenge to robust mooring design for the growing industry of wave energy conversion. We present a discontinuous Galerkin formulation using a local Lax-Friedrich Riemann solver to capture snap loads in mooring cables with high accuracy. An  $hp$ -adaptive scheme is used to dynamically change the mesh size  $h$  and the polynomial order  $p$ , based on the local solution quality. We implement an error indicator and a shock identifier to capture shocks with slope-limited linear elements, while using high-order Legendre polynomials for smooth solution regions. The results show exponential error convergence of order  $p + 1/2$  for smooth solutions. Efficient and accurate computations of idealised shock waves in both linear and nonlinear materials were achieved using  $hp$ -adaptivity. Comparison with experimental data gives excellent results, including snap load propagation in a mooring chain. Application on a wave energy device using coupled simulations highlights the importance of the touch-down region in catenary moorings. We conclude that the formulation is able to handle snap loads with good accuracy, with implications for both maximum peak load and fatigue load estimates of mooring cables.

## 1. Introduction

Snap loads are an important factor in the structural design of marine cable installations. For example, they need to be considered during marine lifting operations (Bauduin et al., 2015) and they are known to cause mooring line failure for floating oil production installations (Safetec, 2013). The snap phenomenon can result in high peak loads and increased fatigue damage of cable installations. For the emerging field of wave energy converters (WECs) that put larger demands on the mooring system design and functionality (Johanning et al., 2007; Fitzgerald, 2009), snap loads are potentially an even larger hazard to the design. Reports show that snap loads can cause great damage in both experiments and field tests of WECs (Hann et al., 2015; Thies et al., 2012; Harnois, 2014; Savin et al., 2012). However, firm conclusions on snap load occurrence and the resulting amplitude is difficult to reach from measurements only (Harnois, 2014). It is therefore important that numerical methods used for cable dynamics are able to handle snap loading events properly.

Snap loads are characterised by a discontinuity in tension magnitude that propagates along the cable (Dhanak and Nikolaos, 2016). There are three main mechanisms by which snap loads are generated in mooring

cables. First, there is the shock wave build up due to nonlinear material response. Tjavaras (1996) studied these shock conditions in highly extensible fibre ropes using the method of characteristics and finite differences. He showed how shocks form in fibre ropes with exponential strain-tension behaviour. A second snap load generation mechanism arises from sea-bed contact, predominantly in catenary slack moorings. Triantafyllou et al. (1985) has showed that a snap is generated when the touch-down point velocity of a chain exceeds the wave-speed in the transverse direction of the cable. This was later observed in experiments by Ref. Gobat and Grosenbaugh (2001) and computed with good results by Ref. Gobat (2000) using finite differences and adaptive time-stepping. The third and most common snap load is however associated with the cable slack condition. The snap load amplitude is in this case dependent on the material stiffness and the local strain rate of the cable at the instant it re-enters the tensioned regime (Hennessey et al., 2005). The experiments of Fylling and Wold (1979) investigated snap loads of this type. They have been numerically studied by several authors, e.g. Shin (1991) using a clipping model that showed that the snap amplitude decreased with increasing free-falling velocity of the cable. Also Vassalos and Kourouklis (1998) used the lumped mass method as described in

<sup>\*</sup> Corresponding author.

E-mail address: [johannes.palm@chalmers.se](mailto:johannes.palm@chalmers.se) (J. Palm).

<sup>1</sup> Currently at Department of Civil Engineering, Aalborg University, Denmark.

Ref. Huang (1994) to compare with said experiments. Good results were obtained for cases with smooth dynamic response, but errors up to 30% were noted for cases with snap loads. We note that in the case of cable slack at the contact point, these definitions overlap and the governing mechanism for the snap is a mixture of the second and third types of snap load generation.

There are a multitude of numerical cable formulations and models; see e.g. Ref. Spak et al. for a good review and Brown and Mavrakos (1999) for a comparative benchmark test between different methods. A common cable discretisation technique is to use discrete lumped masses. This was originally described by Ref. Walton and Polachek (1959), and is frequently used today (Orcina Inc, 2012; ANSYS Inc, 2013). In early work, a number of investigations were also made using finite differences (Tjavaras, 1996; Gobat and Grosenbaugh, 2001; Ablow and Schechter, 1983; Mavrakos et al., 1996). Linear finite element formulations include the work of Aamo and Fossen (2000), and commercial solvers such as DeepC (DNV GL, 2014). A Galerkin method based on cubic splines was introduced by Ref. Buckham et al. (2004) as a starting point to higher order modelling of the cables. Of particular importance to this work is the paper of Montano et al. (2007) who formulated a mixed high-order finite element model for cables. The position and velocity of the cable were modelled using continuous Galerkin finite elements of high order, but the tension was an auxiliary discontinuous Lagrangian multiplier constraint. Under the assumption of negligible bending stiffness, they showed good results for very stiff and inextensible cables. However, to propagate snap loads we need to resolve the time-scales of longitudinal waves of tension. This was the aim of our previous study, where we developed a local discontinuous Galerkin (LDG) method for mooring cables (Palm et al., 2013). The LDG formulation required stabilisation penalty terms as expected (Cockburn and Shu, 2001), but showed good results in convergence and validation tests. However, a constant choice of fluxes made snap load capturing difficult, showing a need for a more sophisticated numerical scheme.

The governing equation of mooring cable dynamics is hyperbolic (Tjavaras, 1996; Montano et al., 2007), and shock waves in hyperbolic conservation laws is a well studied topic. The theorems of Lax and Wendroff (1960), and of Hou and Le Floch state that any converging solution of a shock in a hyperbolic equation will only converge to the correct (and unique) solution if the problem is formulated in conservative form. Discrete representations of shocks are also subject to Ref. Godunov (1959) theorem stating that all constant flux schemes of orders greater than one will produce non-physical extrema (over/undershoots) in the presence of discontinuities. The total variation diminishing (TVD) family of flux-limiters (see e.g. Ref. Sweby (1984)) have been developed to remedy the accuracy for second order finite volume simulations.

Shocks can be modelled accurately using discontinuous Galerkin (DG) methods in conservative form. The DG method is essentially a finite volume scheme with each cell approximated using finite elements. The elements are connected via numerical fluxes, like in the finite volume method. Shape functions of arbitrary polynomial order can be used to achieve exponential convergence for smooth solutions (Karniadakis and Sherwin, 2003), enabling engineering accuracy with only a few elements. However, in the presence of shocks, the estimated amplitude will be affected by overshoots and undershoots around the shock front of the solution (Toro, 2001). There are many approaches to capture shocks, where the main is through limiting the flux (or slope) of the solution as in finite volume schemes, see e.g. Ref. Sweby (1984). Among other techniques we note the artificial viscosity for sub-cell shocks by Ref. Persson and Peraire (2006) and the moment limiters for high order meshes (Krivodonova, 2007). These measures have in several studies been combined with mesh adaptivity in element density ( $h$ ) and/or polynomial order of the expansion basis ( $p$ ) (Berger and Colella, 1989; Bey et al., 1996; Eskilsson, 2011), as well as with shock detection schemes (Bernard, 2008; Krivodonova et al., 2004).

We present a high-order discontinuous Galerkin (DG) method for cable dynamics with the purpose of capturing and resolving snap loads. The problem is formulated in conservative form, including an

approximative Riemann solver based on the local Lax-Friedrich flux. Further, an  $hp$ -adaptive strategy based on the tension magnitude is applied. The  $hp$ -adaptivity aims to utilise the desirable accuracy of high-order elements in smooth regions, while returning to slope limited linear elements around the discontinuities, to resolve the shocks. Computational results are compared with analytic results for three idealised test cases. Further, we compare computational results with experimental data from a mooring chain subjected to prescribed end-point motion.

The paper is organised as follows. First we present the governing equations, recasted in conservative form, and the physical assumptions made in the derivation (Section 2). This is followed by an eigenvalue analysis of the model system (Section 3). Section 4 describes the details of the numerical model implementation, with the  $hp$ -adaptive strategy presented in the following Section 5. Computational examples are then presented in Section 6 and the paper ends with concluding remarks in Section 7.

## 2. Governing equations

For a cable of length  $L_c$ , we use the unstretched cable coordinate  $s \in [0, L_c]$  to express the global coordinate position vector of the cable as  $r = [r_1(s), r_2(s), r_3(s)]^T$ . Under the assumption of negligible bending stiffness, the equation of motion becomes

$$\gamma_0 \ddot{r} = \frac{\partial}{\partial s} (T\hat{t}) + f, \quad (1)$$

$$\hat{t} = \frac{\partial r}{\partial s} \left| \frac{\partial r}{\partial s} \right|^{-1}, \quad (2)$$

where  $\gamma_0$  is the cable mass per unit length,  $T$  is the cable tension force magnitude,  $\hat{t}$  is the tangential unit vector of the cable and  $f$  represents all external forces. For notation we use  $\dot{x} = \frac{\partial x}{\partial t}$  to indicate time derivatives and  $|x| = \sqrt{x_i x_i}$  to denote the  $L_2$ -norm of a vector quantity  $x$ , Vector components are denoted by their index as  $x_i$ ,  $i \in [1, 2, 3]$ , and summation over repeated indices is implied.

Written as a first order system in terms of the cable position  $r$ , its spatial derivative  $q = \frac{\partial r}{\partial s}$  and its momentum density  $\nu = \dot{r}\gamma_0$ , eq. (1) becomes

$$\dot{r} = \frac{\nu}{\gamma_0}, \quad (3)$$

$$\dot{q} = \frac{\partial}{\partial s} \left( \frac{\nu}{\gamma_0} \right), \quad (4)$$

$$\dot{\nu} = \frac{\partial}{\partial s} (T\hat{t}) + f, \quad (5)$$

where we have assumed that the cable mass is constant in time. In terms of a state vector  $u = [r, q, \nu]^T$  the conservative form of the problem is written as

$$\dot{u} = \frac{\partial F(u)}{\partial s} + Q(u), \quad (6)$$

with a flux function

$$F(u) = \left[ \emptyset, \frac{\nu}{\gamma_0}, T\hat{t} \right]^T, \quad (7)$$

and a non-linear source term

$$Q(u) = \left[ \frac{\nu}{\gamma_0}, \emptyset, f \right]^T. \quad (8)$$

### 2.1. External forces

All external forces acting on the cable from the surrounding fluid are grouped in the forcing term  $f$  of eq. (1). The total force is given by

$$f = f_A + f_B + f_C + f_D, \quad (9)$$

where  $f_A$  is the added mass and Froude-Krylov forces,  $f_B$  is the net force of gravity and buoyancy,  $f_C$  represent contact forces, typically from sea-floor interaction, and  $f_D$  is the drag force.

To describe the external forces, we introduce the tangential and normal projection of a vector  $x$  respectively as

$$x_t = x \cdot \hat{t}, \quad (10)$$

$$x_n = x - x_t. \quad (11)$$

In terms of the fluid velocity  $v_f$ , we also let the relative velocity and acceleration of the fluid with respect to the cable be

$$v^* = v_f - \dot{r}, \quad (12)$$

$$\dot{v}^* = \dot{v}_f - \ddot{r}. \quad (13)$$

Then

$$f_A = A_c \rho_f \left( \dot{v}_f + C_{Mn} v_n^* + C_{Mt} v_t^* \right), \quad (14)$$

$$f_B = g \frac{\rho_c - \rho_f}{\rho_c} \gamma_0, \quad (15)$$

$$f_D = 0.5 \rho_f d_c \sqrt{1 + \varepsilon} (C_{Dn} |v_n^*| v_n^* + C_{Dt} |v_t^*| v_t^*), \quad (16)$$

where  $g$  is the gravitational acceleration,  $\varepsilon$  is the axial strain,  $C_{Mn}$ ,  $C_{Mt}$  are the added mass coefficients of the normal and tangential direction respectively, and where  $C_{Dn}$ ,  $C_{Dt}$  are the drag coefficients of the normal and tangential direction. The drag forces and added masses are computed using Morison's formulas (Morison et al., 1950) for a circular cross-section with volume-preserving properties during axial strain. Since the effects of cross-section contraction and axial elongation cancel during uni-axial strain of a volume-preserving material, there is no strain dependence on  $f_A$  and  $f_B$ . For  $f_D$  however, the linear increase with increasing strain  $(1 + \varepsilon)$  is not fully cancelled by the contraction factor for the diameter  $(\sqrt{1 + \varepsilon})^{-1}$ .

The most common contact force,  $f_C$ , in our application comes from the sea floor interaction with the cable. Being a stiff point in the problem, the implementation of the ground model has a potentially large influence on the quality of the simulation. In this paper we use a simple bi-linear spring/damper model in the normal direction of the contact plane. The implementation is close to that used in Ref. Orcina Inc (2012). A tangential friction model from (Lindahl, 1984) using dynamic friction is also implemented. For a horizontal sea floor with a  $(x, y, z)$  coordinates corresponding to vector index 1, 2 and 3 respectively, the contact force is computed as

$$f_C = \begin{cases} G_z + G_{xy} & \text{if } (z_G - r_z) \geq 0, \\ 0 & \text{otherwise,} \end{cases} \quad (17)$$

$$G_z = \left( K_G d_c (z_G - r_z) - 2 \xi_G \sqrt{K_G \gamma_0 d_c} \max(\dot{r}_z, 0) \right) \hat{z}, \quad (18)$$

$$G_{xy} = \mu f_{Bz} \tanh\left(\frac{\pi \dot{r}_{xy}}{v_\mu}\right) \frac{\dot{r}_{xy}}{|\dot{r}_{xy}|} \quad (19)$$

where indices  $\hat{xy}$ , and  $\hat{z}$  denote the horizontal and vertical projections of

a vector respectively. Further,  $r_z$  is the vertical coordinate of the cable position,  $z_G$  is the vertical position of the ground,  $K_G$  is the ground stiffness,  $\xi_G$  is the ratio of critical damping for the ground–cable pair. The coefficient of kinetic friction is in eq (19) denoted as  $\mu$ , with a corresponding velocity of maximum friction  $v_\mu$ .

Please notice that to model the ground interaction as described in eq. (17), we need the position of the cable  $r$  as an independent variable, which is why it is included as an independent variable in eq. (3).

### 3. Eigenvalue analysis

Returning to the model problem in eq. (6). It can be rewritten using the chain rule as

$$\dot{u}_m = J_{mn} \frac{\partial u_n}{\partial s} + Q_n, \quad (20)$$

$$J_{mn} = \frac{\partial F_m}{\partial u_n}, \quad (21)$$

where  $J_{mn}$  is the Jacobian matrix and  $m, n \in [1, 2, \dots, 9]$ . As the flux function  $F$  is independent on the cable position  $r$ ,  $J$  is trivially 0 for dependence on  $r$ . We therefore concentrate our analysis on a reduced six-by-six matrix  $A$ , defined as a sub-matrix in the overall jacobian  $J$

$$J = \begin{pmatrix} \emptyset & \emptyset \\ \emptyset & A \end{pmatrix}. \quad (22)$$

$A$  includes the dependencies of  $F$  on  $q$  and  $\nu$ , which by extension includes a state dependence of the tension force magnitude  $T = T(u)$ . This depends in turn on the material model of the cable. For the purpose of the present analysis, we let the tension force magnitude  $T$  be a differentiable function of the engineering strain in the cable:

$$T = T(\varepsilon), \quad (23)$$

$$\varepsilon(q) = |q| - 1, \quad (24)$$

$$\frac{\partial \varepsilon}{\partial q_j} = \frac{q_j}{|q|}, \quad (25)$$

so that

$$\frac{\partial}{\partial q_j} \left( \frac{T q_i}{|q|} \right) = \delta_{ij} \frac{T}{|q|} + \left( \frac{\partial T}{\partial \varepsilon} - \frac{T}{|q|} \right) \frac{q_i q_j}{|q|^2}. \quad (26)$$

Thus, for  $i, j \in [1, 2, 3]$ , the six-by-six matrix  $A$  becomes

$$A = \gamma_0 \begin{pmatrix} \emptyset & \frac{\delta_{ij}}{\gamma_0^2} \\ \delta_{ij} c_n^2 + \frac{q_i q_j}{|q|^2} (c_t^2 - c_n^2) & \emptyset \end{pmatrix}, \quad (27)$$

where

$$c_n^2 = \frac{T}{|q| \gamma_0}, \quad c_t^2 = \frac{\frac{\partial T}{\partial \varepsilon}}{\gamma_0}, \quad (28)$$

are introduced as the cable celerities in the normal and tangential direction respectively. These are also the eigenvalues of  $A$ :

$$\lambda_A = [-c_n, -c_n, c_n, c_n, -c_t, c_t]^T. \quad (29)$$

As  $\lambda_A \in \mathbb{R}$ , we have confirmed that our system is indeed hyperbolic provided that the tension is non-negative. Cables under negative tension without bending stiffness makes the problem ill-posed (Triantafyllou

et al., 1985). Physically we now expect six waves to propagate in the cable: 4 transverse waves (2 left-going and 2 right-going) and 2 longitudinal waves (1 left-going and 1 right-going).

#### 4. Discontinuous Galerkin method

We apply eq. (6) on a cable domain  $\Omega$  of unstretched coordinate  $s \in [0, L_c]$ .  $\Omega$  is discretised in to a set of  $N$  elemental regions  $\Omega^e$  of mesh size  $h^e$ , within which an arbitrary function  $y(s, t)$  is approximated as a Legendre polynomial of order  $p$ :

$$y(s, t) \approx y^e(s, t) = \sum_{k=0}^{k=p} \phi_k(s) \tilde{y}_k^e(t). \quad (30)$$

here  $\tilde{y}_k^e$  is the  $k^{th}$  expansion coefficient corresponding to the basis function of order  $k$ ,  $\phi_k(s)$ . The discontinuous Galerkin (DG) formulation of eq. (6) is then

$$\left( \phi_k, \frac{\partial u^e}{\partial t} \right)_{\Omega^e} = \left( \phi_k, \frac{\partial F^e}{\partial s} \right)_{\Omega^e} + (\phi_k, \mathcal{Q}^e)_{\Omega^e}, \quad \forall k \in [0, p], \quad (31)$$

using

$$(a(s, t), b(s, t))_{\Omega^e} = \int_{\Omega^e} a(s, t) b(s, t) ds,$$

to denote the inner product operator on the elemental domain. An integration by parts of the weak derivative term  $\left( \phi_k, \frac{\partial F^e}{\partial s} \right)_{\Omega^e}$ , allows eq. (31) to be written

$$\left( \phi_k, \frac{\partial u^e}{\partial t} \right)_{\Omega^e} = - \left( \frac{\partial \phi_k}{\partial s}, F^e \right)_{\Omega^e} + [\phi_k \widehat{F^e}]_{s_L^e}^{s_U^e} + (\phi_k, \mathcal{Q}^e)_{\Omega^e}, \quad \forall k \in [0, p]. \quad (32)$$

here  $s_U^e$  and  $s_L^e$  denote the elemental upper and lower bounds of the unstretched cable domain coordinate  $s$  respectively. The key step of the DG method is how the resulting boundary integral in eq. (32) has been approximated with a numerical flux  $\widehat{F^e}$ . As the elements are discontinuous at the element boundaries, the numerical flux provides the coupling between neighbouring elements. An additional integration by parts, without a numerical approximation of the boundary term, recasts eq. (32)  $\forall k \in [0, p]$  as

$$\left( \phi_k, \frac{\partial u^e}{\partial t} \right)_{\Omega^e} = \left( \phi_k, \frac{\partial F^e}{\partial s} \right)_{\Omega^e} + [\phi_k (\widehat{F^e} - F^e)]_{s_L^e}^{s_U^e} + (\phi_k, \mathcal{Q}^e)_{\Omega^e}. \quad (33)$$

Finally we use the separation of time and space dependence defined in eq. (30) to rewrite eq. (33) in terms of the modal coefficients of our polynomial space:

$$(\phi_k, \phi_i) \frac{\partial \tilde{u}^e}{\partial t} = \left( \phi_k, \frac{\partial \phi_i}{\partial s} \right) \tilde{F}^e + [\phi_k (\widehat{F^e} - F^e)]_{s_L^e}^{s_U^e} + (\phi_k, \mathcal{Q}^e)_{\Omega^e} \quad (34)$$

$$\forall k, i \in [0, p]$$

##### 4.1. Local Lax-Friedrich flux

The numerical fluxes,  $\widehat{F^e}$  are for all internal element boundaries evaluated by the local Lax-Friedrich (LF) flux as defined e.g. in (Bernard, 2008):

$$\widehat{F^e} = \{F^e\} + |\lambda|_{max} [[u^e]] \text{ on } \Gamma \in \Omega. \quad (35)$$

Notations  $\{x^e\}$  and  $[[x^e]]$  are

$$\{x^e\} = 0.5(x^+ + x^-), \quad (36)$$

$$[[x^e]] = 0.5(n^+ x^- + n^- x^+), \quad (37)$$

where  $x^+$  means taking the value from the internal side of the boundary and  $x^-$  from the neighbouring element. The normal vector  $n$  refers to the outward pointing normal, defined for each element boundary as  $n^+ = -1$  on  $s_L^e$  and as  $n^+ = 1$  on  $s_R^e$ . The maximum eigenvalue needed in eq. (35) is in this work chosen for each equation as:

$$|\lambda|_{max} = \begin{cases} \max(|c_n(u^-)|, |c_n(u^+)|) & \text{if } u = q \\ |c_i| & \text{otherwise} \end{cases}. \quad (38)$$

This means that when  $T \rightarrow 0$ , the LF flux approaches a simple centred scheme for the  $q$ -equation (4), while remaining upwinded for eqs. (3) and (5).

##### 4.2. Boundary conditions

Domain boundaries are separated into Dirichlet (D) and Neumann (N) type. Dirichlet conditions control the position and the momentum (from velocity conditions), and Neumann conditions affect the tension force vector  $T\hat{t}$ . On domain boundaries, the fluxes are chosen as

$$F^- = [\emptyset, v_D, (T\hat{t})^+]^T \text{ on } \Gamma_D, \quad F^- = [\emptyset, \frac{\nu^+}{\gamma_0}, (T\hat{t})_N]^T \text{ on } \Gamma_N \quad (39)$$

$$u^- = [r_D, q^+, v_D \gamma_0]^T \text{ on } \Gamma_D, \quad u^- = [r^+, |q^+| \hat{t}_N, \nu^+]^T \text{ on } \Gamma_N \quad (40)$$

where again  $^+$  indicates taking the value from the internal side of the boundary. We note that a prescribed tension force vector boundary condition is weakly modelled in the  $q$  equation. The condition enforces the correct direction of the force, but maintains the norm of the inner field. The tension magnitude is instead enforced through the force flux in the momentum equation.

##### 4.3. Time integration

Eq. (34) is advanced in time with the strong-stability-preserving third-order explicit Runge-Kutta scheme, as implemented in Ref. Cockburn and Shu (2001). If  $\tilde{u}_k$  is the solution set of modal coefficients at time  $t_k$ , and  $\mathbf{L}(\tilde{u}) = \frac{\partial \tilde{u}}{\partial t}$  represents the semi-discrete operator for the time derivative of the solution, then

$$\begin{aligned} \tilde{u}^{(1)} &= \tilde{u}_k + \Delta t \mathbf{L}(\tilde{u}_k), \\ \tilde{u}^{(2)} &= \frac{3}{4} \tilde{u}_k + \frac{1}{4} (\tilde{u}^{(1)} + \Delta t \mathbf{L}(\tilde{u}^{(1)})), \\ \tilde{u}_{k+1} &= \frac{1}{3} \tilde{u}_k + \frac{2}{3} (\tilde{u}^{(2)} + \Delta t \mathbf{L}(\tilde{u}^{(2)})), \end{aligned}$$

where  $\Delta t = t_{k+1} - t_k$ .  $\tilde{u}^{(1)}$  and  $\tilde{u}^{(2)}$  represent intermediate solutions of the algorithm.

#### 5. Adaptivity

The goal of the adaptive mesh refinement scheme is to limit the discretisation error to below a pre-set tolerance level,  $\epsilon^*$ . To do this we need an indicator of the relative error, a smoothness indicator to let us know which type of error that we observe, and a mechanism to efficiently adapt the spatial discretisation to best fit the solution.

##### 5.1. Error indicator

In this work, we use the tension force magnitude  $T$  as indicator variable for the quality of the solution. Any other locally available variable could theoretically be chosen, but the strong nonlinear impact of  $T$  on the

solution, and the fact that it is scalar-valued, makes it a suitable and computationally efficient choice. For smooth solutions, we expect a convergence rate of  $\mathcal{O}(h^{p+1})$ , but close to discontinuities the solution converges as  $\mathcal{O}(h)$  (Krivodonova et al., 2004). Several authors have suggested to use the elemental jump of the solution as a measure of the numerical error (Bernard, 2008; Krivodonova et al., 2004; Barter and Darmofal, 2010). Barter and Darmofal (2010) used the relative jump

$$\tau = \frac{[[T]]}{\{T\}},$$

at element edges to indicate regions of shocks. In this paper, we incorporate the relative jump into Bernard's estimation for the relative error (Bernard, 2008) to get

$$\varepsilon^e = \frac{1}{\sqrt{8}} \sqrt{(\tau_L^e)^2 + (\tau_R^e)^2}, \quad (41)$$

where  $\tau_L^e$  and  $\tau_R^e$  are the relative jumps at the left and right elemental borders respectively.

### 5.2. Shock detection

In order to decide on the nature of the error, i.e. locate regions of sharp gradients or shocks, we follow Krivodonova et al. (2004) and use an intermediate convergence rate  $h^{0.5(p+1)}$  to establish a shock indicator of element  $e$ . Computing

$$I^e = \max(\tau_L^e, \tau_R^e) h^{-0.5(p+1)}, \quad (42)$$

which rapidly grows to infinity close to discontinuities and is small in smoother regions, results in the shock criteria as  $I^e \geq 1$  (Krivodonova et al., 2004). In our case, we also need to treat specially the cable slack condition, where  $T \rightarrow 0$ . When this happens, a snap load is expected to occur in the near future, and we therefore treat it as a shock criteria. Thus, we also introduce a low-tension criteria  $T^*$ , that indicate shock behaviour if  $\min(T^e) \leq T^*$ , with  $\min(T^e)$  evaluated at the quadrature points of element  $e$ . The shock criteria and detectors are combined into the shock detecting function  $S^e$  as

$$S^e = \begin{cases} 1 & \text{if } I^e \geq 1 \text{ and } \varepsilon^e \geq \varepsilon^* \\ 1 & \text{if } \min(T^e) \leq T^* \\ 0 & \text{otherwise} \end{cases} \quad (43)$$

Please note that the jump-based shock detector is only applied to elements that have errors higher than the tolerance level, while the low tension indicator is applied to all elements in the cable domain.

### 5.3. Adaptivity control

The adaptive strategy aims to take advantage of the superior convergence of  $p$ -refinement compared to  $h$ -refinement for smooth regions. In this work, we therefore let  $p$ -refinement have precedence over  $h$ -refinement in all elements of smooth solution, with errors larger than the tolerance. If shocks are detected, the mesh is forced into maximum  $h$ -refinement and the order is reduced to linear approximation  $p = 1$ .  $h$ -refinement is restricted to splitting elements in half and merging two equally sized elements with the same parent. The initial mesh  $h$ -resolution is not allowed to coarsen, and the splitting hierarchy of elements is therefore confined to one element of the initial mesh.

The inverse operation of coarsening the resolution follows the recipe of Bernard (2008), assuming the error relation between the new and the old mesh to be:

$$\frac{\varepsilon^e}{\varepsilon^*} = \frac{h^{p+1}}{h^{*p+1}}, \quad (44)$$

where  $p^*$  and  $h^*$  denote the resolution parameters in the modified mesh. Thus, for merging elements with constant order  $p$ , the criterion is:  $\varepsilon^e < 0.5^{p+1}\varepsilon^*$ ; and for lowering the polynomial order under constant  $h$ , consequently:  $\varepsilon^e < h\varepsilon^*$ . Combining the above, we arrive at the  $hp$ -adaptive control algorithm

$$\text{if } S^e = 1 : \quad p = 1, \quad h = h_{\min}$$

$$\text{if } S^e = 0 : \quad \begin{cases} p = \min(p + 1, p_{\max}) & \text{if } \varepsilon^e \geq \varepsilon^* \\ h = \max(0.5h, h_{\min}) & \text{if } \varepsilon^e \geq \varepsilon^* \text{ and } p = p_{\max} \\ h = \min(2h, h_{\max}) & \text{if } \varepsilon^e < 0.5^{p+1}\varepsilon^* \\ p = \max(p - 1, 1) & \text{if } \varepsilon^e < h\varepsilon^* \text{ and } h = h_{\max} \end{cases},$$

where  $S^e$  is the shock indicator function explained in eq. (43). The application of the control algorithm to pure  $h$  is straightforward, as we simply skip the  $p$ -adaptation parts. For pure  $p$  refinement, we skip the  $h$ -adaptation as well as the shock detection step. The adaptive scheme is applied after a complete time step, so that all stages of the Runge-Kutta scheme share the same spatial resolution.

### 5.4. Slope limiting

Having a working  $hp$ -adaptive scheme to properly resolve the snap loads, we need to limit the unwanted overshoots close to these sharp gradients. We apply the limiter as

$$\tilde{u}_1^e = \minMod\left(\theta_l \frac{\tilde{u}_0^e - \tilde{u}_0^{e-1}}{2}, \theta_l \frac{\tilde{u}_0^{e+1} - \tilde{u}_0^e}{2}, \tilde{u}_1^e\right), \theta_l \in [1, 2], \quad (45)$$

where  $\tilde{u}_0^e$  is the mean value and  $\tilde{u}_1^e$  is the linear slope of element  $e$ . The min-mod function is defined as

$$\minMod(a, b, c) = \begin{cases} \min(a, b, c) & \text{if } a, b, c > 0 \\ \max(a, b, c) & \text{if } a, b, c < 0 \\ 0 & \text{otherwise} \end{cases}.$$

The value of  $\theta_l$  blends the limiter between the classical min-mod for  $\theta_l = 1$  and the less restrictive, generalised min-mod from (Cockburn and Shu, 2001) for  $\theta_l = 2$ . The limiter is applied after each stage of the Runge-Kutta time-stepping scheme.

The limiter is active on all elements of order  $p = 1$  in the domain, which for a pure  $h$ -refining simulation tends to dampen smooth extrema (Cockburn and Shu, 2001). This problem is circumvented in our  $hp$ -adaptive simulations, where  $p$ -refinement has precedence in regions without shocks. This leads to that smooth extrema are resolved using few elements of higher order, where the limiter is disabled by default.

## 6. Computational results

All results from computational test cases presented in this section are using the Legendre polynomials as modal bases. For the convergence studies, we use the  $L_2$  norm to quantify the errors of our solution. This is defined by the element integral over the error at the Gauss-Lobatto-Legendre (GLL) quadrature points. Seventeen quadrature points were used for each element giving exact integration up to  $p = 15$  (Karniadakis and Sherwin, 2003). Time step size is in this adaptive case conveniently defined in fractions of the maximum allowed time step CFL number in the mesh. The CFL of an element used in this work is defined by:

$$CFL = \frac{1}{c_t} \begin{cases} \frac{h}{2p+1} & \text{if } p < 3 \\ hp^{-2} & \text{otherwise} \end{cases}. \quad (46)$$

6.1. Vibrating string: spatial convergence

The spatial convergence of the formulation is confirmed by a two-dimensional benchmark. We studied the  $L_2$  error of position and velocity of a linear standing wave with fixed end points and constant tension force magnitude  $T$ . No external forces were applied. The analytic solution of this problem is taken from Ref. Greiner (2003):

$$r_z(s, t) = A \cos\left(\frac{c_u \pi}{L_c} t\right) \sin\left(\frac{\pi}{L_c} s\right), \quad (47)$$

with initial amplitude  $A = 1$  m and unstretched cable length  $L_c = 100$  m. The celerity in the normal direction of the unstretched domain,  $c_u$ , is here computed from the cable mass per meter ( $\gamma_0 = 0.1 \text{ kg m}^{-1}$ ), the pre-strain ( $\epsilon_0 = 0.1$ ), and the tension force ( $T_0 = 1, 100 \text{ N}$ ) as

$$c_u = \sqrt{\frac{T_0}{\gamma_0(1 + \epsilon)}} = 100 \text{ ms}^{-1}. \quad (48)$$

The initial conditions of the cable was a constant prestrain in the horizontal direction and an initial vertical displacement of  $r_z(s, 0) = A \sin\left(\frac{\pi}{L_c} s\right)$ . The computed result after one full period of oscillation was compared with the analytic values. Results of different mesh resolutions of  $h$  and  $p$  are shown in Fig. 1 and in Table 1. For  $p \in [1, 4]$ , we used  $N = 5, 10, 20, 40$  elements respectively to establish the convergence rate. In Fig. 1, results from  $p \in [1, 15]$  on  $N = 2$  and  $N = 3$  element meshes are also shown. The time step size was in this case constant and was chosen sufficiently small not to affect the accuracy of the simulation. From Table 1, we conclude the convergence rate to be  $p + 1/2$ . This gives confidence that the formulation is correctly implemented, and that the discretisations in both time and space are working as expected.

6.2. Propagating shock: linear material

A one-dimensional test case with a discontinuous initial condition is used to test the adaptive scheme described in Section 5. A  $L = 100$  m cable is horizontally suspended over 115 m in the absence of external forces. The cable mass is  $\gamma_0 = 1 \text{ kg m}^{-1}$  and the cable material is linear-elastic with axial stiffness  $EA = 10 \text{ kN}$ . The cable is initially at rest with a discontinuous pre-strain:

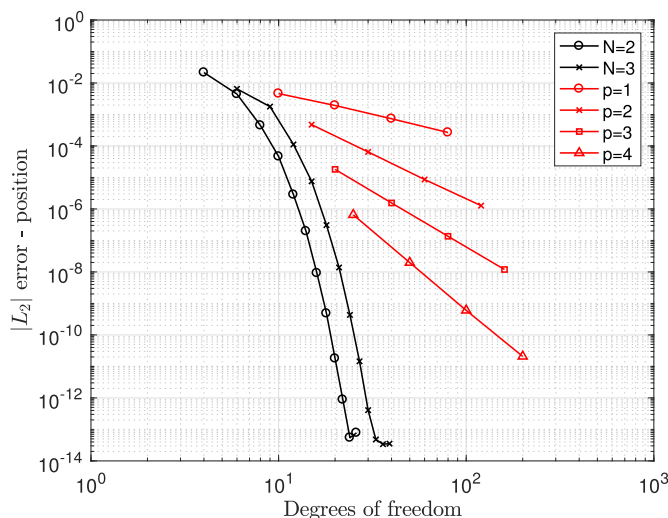


Fig. 1. The error in the  $L_2$  norm of the cable position after 1 full period of oscillation as a function of degrees of freedom in the discretisation. Shown in logarithmic scale.

Table 1

Convergence rates for the linear standing wave for variables position,  $r$ , and velocity,  $v$ .

variable	$p$	$N = 10$	$N = 20$	$N = 40$		
		error	error	order	error	order
$r$	1	2.13 E-3	7.65 E-4	1.48	2.73 E-4	1.48
	2	1.03 E-4	1.30 E-5	3.00	1.63 E-6	2.99
	3	1.57 E-6	1.36 E-7	3.52	1.20 E-8	3.51
	4	3.75 E-8	1.08 E-9	5.12	3.05 E-11	5.14
$v$	1	1.54 E-3	4.14 E-4	1.89	1.31 E-4	1.66
	2	5.32 E-4	1.14 E-4	2.22	2.13 E-5	2.42
	3	6.47 E-7	4.63 E-8	3.81	3.71 E-9	3.64
	4	2.08 E-7	1.10 E-8	4.25	5.09 E-10	4.43

$$\epsilon_0 = \begin{cases} 0.1 & \text{if } s < 0.5L \\ 0.2 & \text{if } s > 0.5L \end{cases}$$

The evolution of the shock front over the first second is shown in Fig. 2.

Fig. 3(a) shows the initial step tension, plotted at the quadrature points of an  $h$ -adapted mesh from  $N = 10, p = 1$  elements in 5 levels. Fig. 3 shows that both the adapted solution and the equivalent static resolution of  $N = 320, p = 1$  are capable of capturing the shock well. The accuracy is strictly dependent on the finest mesh size, and the results show very small differences between the static and the adapted mesh, both for cases with and without limiter applied. Although no difference in accuracy, the  $h$ -adapting mesh is around 5 times faster to compute for this simplified case, as can be seen from Table 2. Of course, the code structure is not optimal for a static mesh, and we treat this more as an upper limit on the speed-up potential for this case. Further, Fig. 3(b) clearly demonstrates the benefits of the generalised minMod limiter of Cockburn and Shu (2001) over the standard minMod and the intermediate  $\theta_l = 1.5$  solution, which are much more diffusive. Simulations were made with time step size of 0.9 CFL for all meshes.

6.3. Propagating shock: nonlinear material

In the case of a nonlinear material response, two important features change in relation to the linear case above. Primarily, the speed of sound is no longer constant, but dependent on the local strain  $c_t = c_t(\epsilon)$ , and secondly, the shock amplitude is no longer preserved during reflection at fixed Dirichlet boundaries. To verify that the correct shock speed and reflection amplification are obtained in the numerical simulations, we implement a nonlinear material response of exponential form,

$$T(\epsilon) = K(e^{a\epsilon} - 1), \quad (49)$$

so that the cable celerity is given by

$$c_t(\epsilon) = \sqrt{\frac{1}{\gamma_0} \frac{\partial T}{\partial \epsilon}} = \sqrt{\frac{Ka}{\gamma_0} e^{a\epsilon}}. \quad (50)$$

We now study a longer cable in one dimension,  $L_c = 1,000$  m, with  $K = 581.9767 \text{ N}$ ,  $a = 10$ .  $\gamma_0$  is still  $1 \text{ kg/m}$ . Starting at a static strain  $\epsilon_s = 0.1$ , corresponding to a  $T_s = 1 \text{ kN}$  static force, the cable is fixed in position at the left end ( $s = 0$ ), and loaded with a prescribed force at the right end ( $s = L_c$ ). An initial step tension is imposed on the right boundary at  $t = 0$ , creating a left-going, initial shock with amplitude  $\delta T_i = T(\epsilon_i) - T(\epsilon_s)$ , where  $\epsilon_i$  is the strain associated with the loading boundary tension  $T_i$ . The theoretically predicted shock speed,  $S$ , is given by

$$S^2 = \frac{1}{\gamma_0} \frac{\delta T}{\delta \epsilon}, \quad (51)$$

where  $\delta T$  is the shock tension amplitude and  $\delta \epsilon$  is the size of the strain discontinuity across the shock. After reflection, the shock amplitude  $\delta T_r$  is

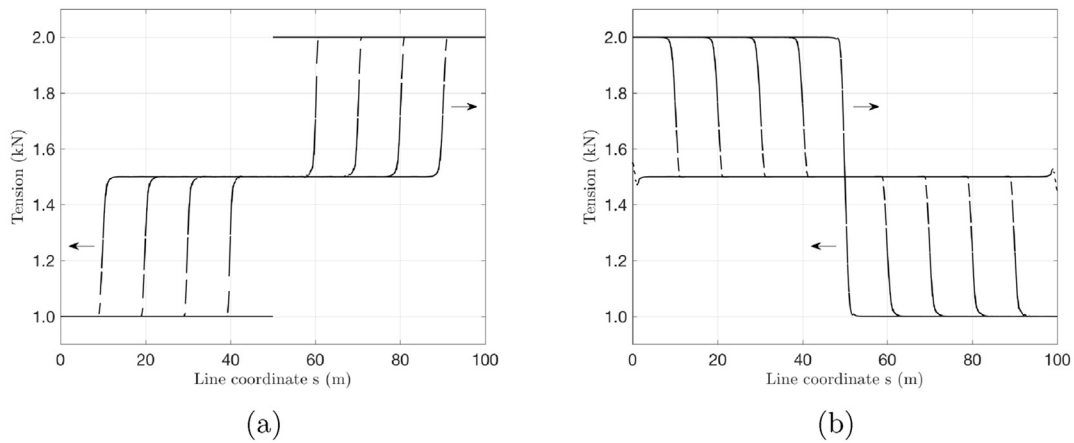


Fig. 2. Shock appearance during the first second of simulation, sampled every 0.1 s from the  $N = 320$  case. (a) shows  $t \in [0, 0.4]$  s and (b) shows  $t \in [0.5, 1.0]$  s, after reflection at the boundaries. The arrows indicate the direction of propagation of the shock front.

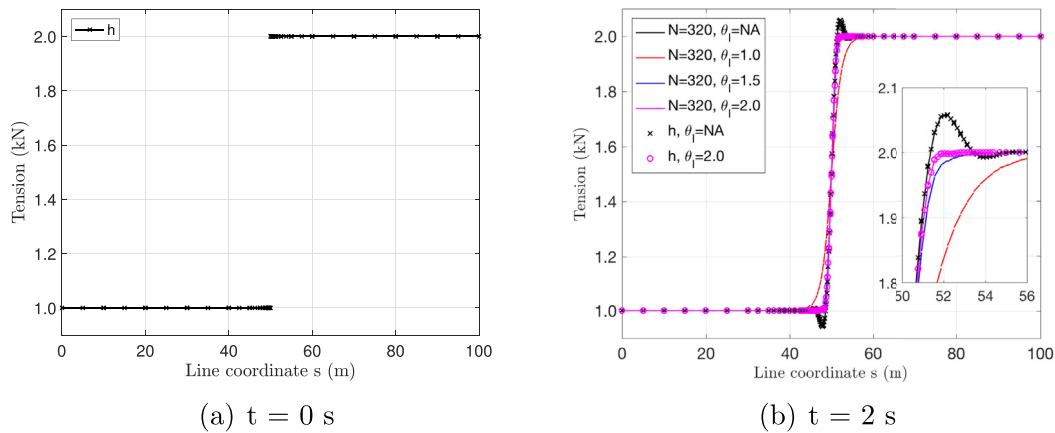


Fig. 3. Shock front appearance. (a): Initial condition of tension, also showing the  $h$ -adapted mesh in 5 levels with markers on quadrature points. (b) Shock front after 1 return period for different values  $\theta_l$  on 320 static linear elements, and the 5-level  $h$ -adapted solutions indicated by markers.

Table 2

Relative computational times for different mesh settings. Simulations were made with a constant CFL condition of 0.9.

Type	$N$	$p$	DoF	$\theta_l$	relative time
static	160	1	320	NA	0.174
static	160	1	320	2.0	0.254
static	320	1	640	NA	0.675
static	320	1	640	2.0	1.000
$h$ -adapting	48	1	96	NA	0.192
$h$ -adapting	43	1	86	2.0	0.208

theoretically predicted from the strain relations across the reflection, as derived by Ref. Tjavaras (1996):

$$\Psi(\epsilon_r) = 2\Psi(\epsilon_i) - \Psi(\epsilon_s), \tag{52}$$

$$\Psi(\epsilon) = \int_0^\epsilon c_t(\epsilon) d\epsilon = \sqrt{\frac{K}{\alpha\gamma_0}} (\sqrt{e^{\alpha\epsilon}} - 1), \tag{53}$$

$$\delta T_r = T(\epsilon_r) - T(\epsilon_i). \tag{54}$$

Fig. 4 shows simulation results with two different initial shock amplitudes,  $\delta T_i = 1$  kN and  $\delta T_i = 2$  kN respectively. The numerical results in this section were obtained using  $hp$ -adaptive meshes with maximum 5

levels of  $h$ -refinement on a  $N = 20$  element base mesh. Time step size is adaptive and chosen from the minimum of 0.9 CFL in the domain. Again, the  $\theta_l = 2.0$  limiter was applied to avoid overshoots of the solution.

The results in Fig. 4 are compared with the analytical shock profiles of both the initial shock and the reflected shock, each after 800 m of propagation from their respective point of origin. Upon returning to the right edge, the shock is transformed to a rarefaction wave in the reflection on the Neumann boundary. The third time state shown in Fig. 4 shows how the rarefaction widens the shock as the leading edge propagates faster than the trailing edge ( $c_t(\epsilon_r) > c_t(\epsilon_i)$ ). The rarefaction is not a shock wave in itself, meaning that each characteristic propagates with the local speed of sound  $c_t(\epsilon)$  and not with the shock speed  $S$  from eq. (51).

The numerical examples match the analytical predictions very well. Both initial and reflected shock amplitudes and speeds of propagation are captured by the numerical scheme. The width of the rarefaction wave front is also correct in the simulations. The numerical results of reflected shock amplitude,  $\delta T_r$ , are shown in Table 3 together with the analytical predictions. The amplification of the reflected shock amplitude exemplifies the intricate coupling between the impact of a snap load and the material in which it propagates.

#### 6.4. Catenary chain dynamics: validation

To validate the formulation, we compare against experimental measurements on a single catenary chain with characteristics as described in

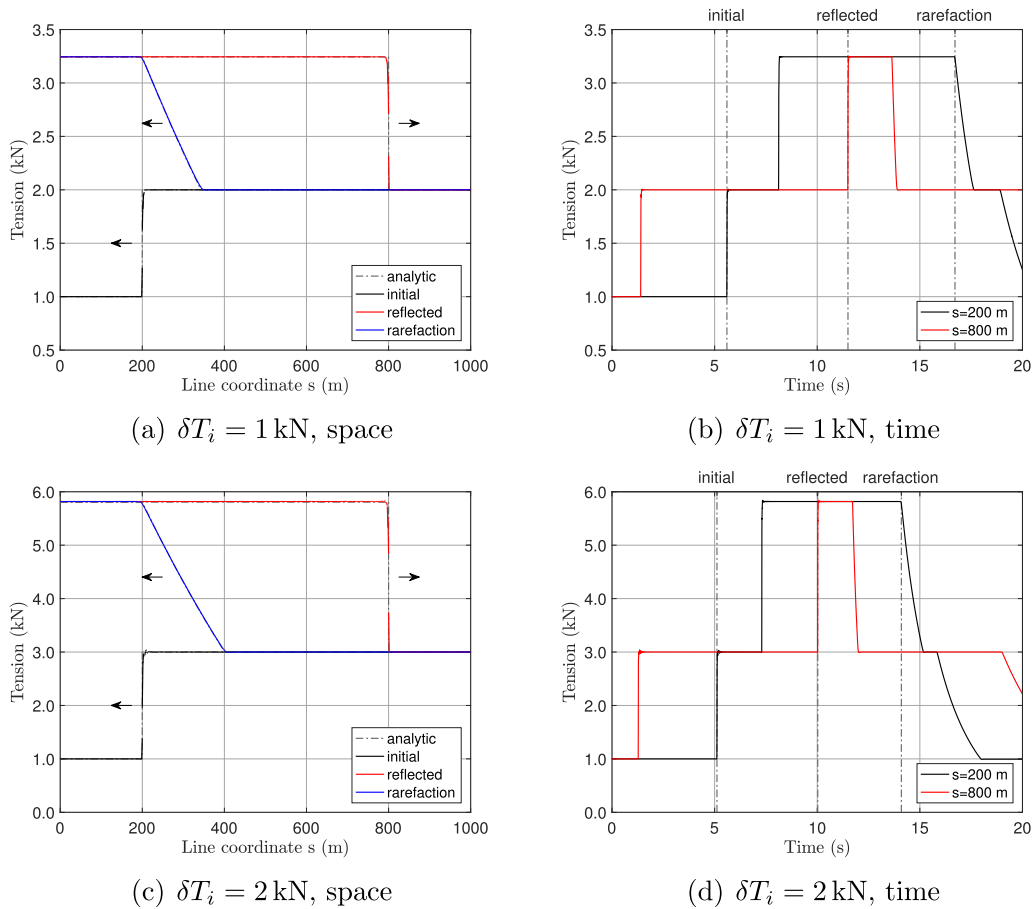


Fig. 4. Shock front appearance in the nonlinear case, studied at two target positions  $s = 200$  m and  $s = 800$  m respectively. The snapshots in (a) and (c) correspond to analytically predicted arrival times of the shock. (b) and (d) show the tension time histories of the two target points. Further, (a)–(b) correspond to the  $\delta T_i = 1$  kN load case, and (c)–(d) correspond to the  $\delta T_i = 2$  kN case.

Ref. Bergdahl et al.. A 33 m chain is suspended in a 3 m deep water tank, with one end anchored to the concrete floor of the tank. If the anchor point is the origin ( $P_A = [x, z] = [0, 0]$ ), the other end (fair-lead) is initially located at  $P_B = [32.554, 3.3]$  m. The cable end-point is subject to a circular motion around  $P_B$  of radius 0.2 m and with two different period times:  $T_{1.25} = 1.25$  s and  $T_{3.5} = 3.5$  s respectively. The chain properties are summarised in Table 4. The cable material response is modelled as bilinear, with no compressive loads allowed. Consequently

$$T = \begin{cases} K_c \epsilon & \text{if } \epsilon > 0 \\ 0 & \text{otherwise} \end{cases} \quad (55)$$

Fig. 5 shows the  $hp$ -adaptive results compared with experimental measurements of the fair-lead tension. Overall there is an excellent agreement between the experimental and computed results. The step-wise increase in fair-lead tension of the  $T_{1.25}$  case, is studied in more detail in Fig. 6(b), where five instants in time (labelled 1–5) are highlighted. Fig. 6(a) shows the corresponding tension along the unstretched cable coordinate  $s$  for each of these times. At 1, the snap has just been generated. This is in agreement with (Triantafyllou et al., 1985; Gobat

Table 3  
Comparison between analytical and numerical results of reflected shock amplitude. Index notations used for strain and shock amplitude are ‘a’: analytical, and ‘n’: numerical. The relative error in reflected tension amplitude is computed from  $\epsilon_{\delta T_r} = (\delta T_r^n - \delta T_r^a) / \delta T_r^a$ .

$\delta T_i$ (kN)	$\epsilon_s$ (-)	$\epsilon_i$ (-)	$\epsilon_r^a$ (-)	$\delta T_r^a$ (kN)	$\epsilon_r^n$ (-)	$\delta T_r^n$ (kN)	$\epsilon_{\delta T_r}$ (-)
1.0	0.1	0.1490	0.1883	1.2437	0.1883	1.2449	0.0004
2.0	0.1	0.1817	0.2396	2.8061	0.2397	2.8171	0.0019

Table 4  
Computational settings used to validate the cable model. Values are taken from Ref. Bergdahl et al.. See Section 2 for a full description of the labels. \* The axial stiffness of the cable is set to 0 when the strain becomes negative.

Label	Value	Unit	Description
$\gamma_0$	0.0818	kg/m	mass per meter
$d_c$	0.0022	m	link diameter
$L_c$	33	m	cable length
$K_c$	10	kN	axial stiffness*
$C_{Mt}$	0	–	tangential added mass.
$C_{Mn}$	3.8	–	normal added mass
$C_{Dt}$	0.5	–	tangential drag
$C_{Dn}$	2.5	–	normal drag
$K_G$	3	GPa/m	ground stiffness
$\xi_G$	1	–	ground damping
$\mu$	0.3	–	ground friction coeff.
$v_\mu$	0.01	m/s	friction velocity
$\Delta t$	0.45CFL	s	adapting time step size

and Grosenbaugh, 2001) who showed that snap loads occur when the transverse motion velocity of the touch down point (TDP) exceeds the transverse wave speed of the cable ( $c_n$ ). In this case, where  $T = 0$ ,  $c_n = 0$  the snap criterion is of course met for any transverse motion of the TDP. We also note some numerical oscillations in the low tension region as the cable has been completely slack. The tension at times 2–4 shows how the snap load is propagating back and forth in the cable, which matches the experimental times very well. The shock amplitude is continuously decreasing as the shock propagates. This is mainly due to the dynamic friction force from the ground and not the hydrodynamic damping from drag. At 5, the peak shock has just been reflected at the fair-lead, and

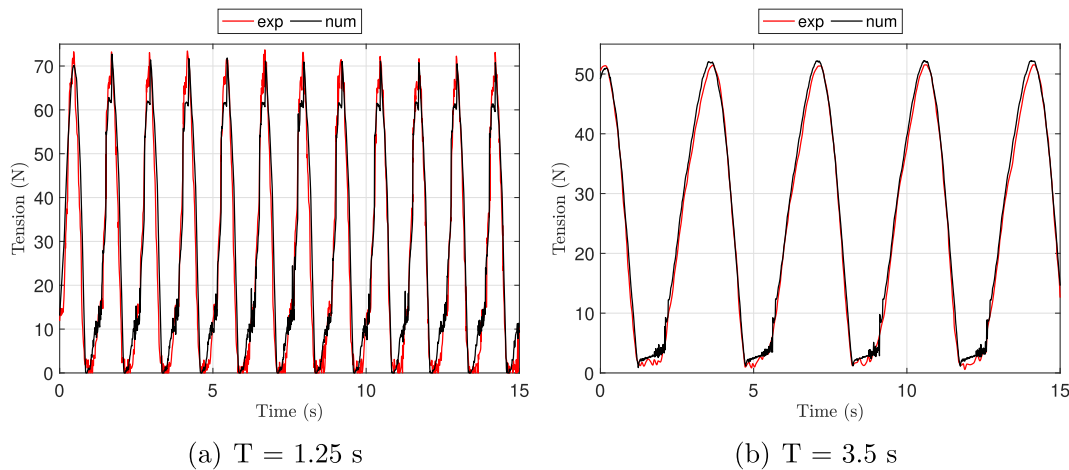


Fig. 5. *hp*-adaptive results of the fair-lead tension magnitude compared with experimental data. The  $T_{1.25}$  and  $T_{3.5}$  simulations were made with 5 and 4 levels of *h*-refinement respectively, from an initial mesh of  $N = 10$  elements.

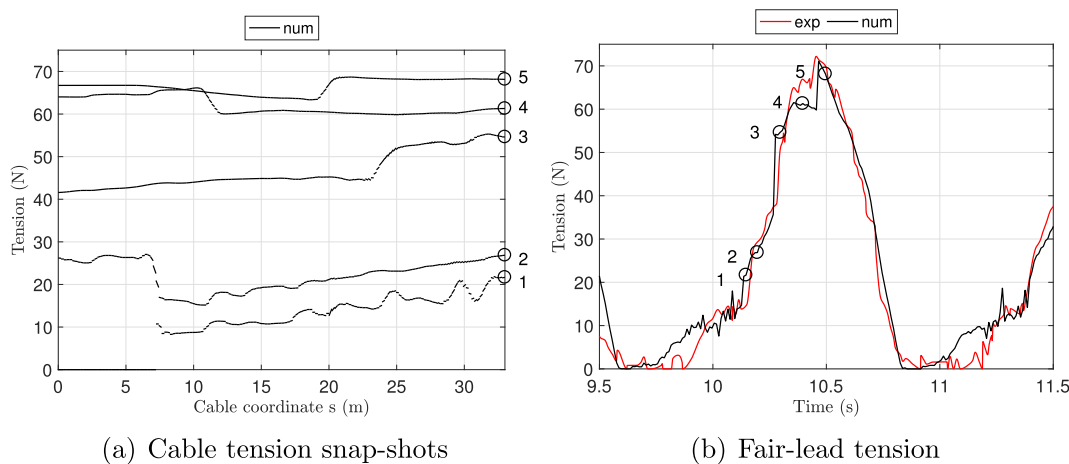


Fig. 6. Explanation of the dynamic properties of the fair-lead tension time history. (a) shows 5 snap shots of the cable tension along the cable length. Graph no. 1 shows the formation of the shock, at  $t = 10.15$  s and numbers 2–5 show the tension force evolution between  $t = 10.15$  s and  $t = 10.45$  s, sampled every 0.1 s. The right figure (b) is a temporal zoom of Fig. 5(a), with the times of the snap shots marked by black circles.

although the peak force matches very well, we note that the shock contribution at the peak is larger in the numerical results than in the experiments. Overall however, Fig. 6 shows that the complicated dynamic behaviour of the cable during the upstroke motion is very well captured by the numerical model.

### 6.5. Catenary chain dynamics: application

As a final example, we present mooring results coupled to a linear radiation-diffraction model of a generic wave energy converter (WEC). The device is taken from Ref. Fitzgerald (2009) as a truncated cylinder, moored with four steel chains. The mooring layout can be seen in Fig. 7(a). In this case, the moorings have a strong impact on the dynamic response of the device, increasing the draft by 13.4 percent in equilibrium. The linear hydrodynamic coefficients for added mass and radiation damping are collected from Nemoh (Babarit and Delhommeau, 2015). The dynamic motion of the moored device was simulated in Wec-Sim (NREL and Sandia Corp, 2015) with an additional coupling module developed for Moody. As we resolve the time-scale of the longitudinal waves in the mooring cables, we have two time-scales in the coupled problem: one for the mooring cables and one for the WEC motion. In between two large time steps of the WEC solver, intermediate mooring boundary conditions for the fair lead positions are generated using a staggered quadratic interpolation of the fair lead position. The coupling

and the interpolation procedure are described in detail in Ref. Palm et al. (2016), where coupled CFD simulations with moorings were validated. The device is also connected to a linear power take off in the heave direction, with constant damping factor  $b_{33} = 15$  kNs/m. The physical properties of the WEC and the mooring cables are summarised in Tables 5 and 6 respectively. The initial position of the attachment point of cable 1 was  $P_1 = [-1.863, 0, -5]$  m, and the anchor was placed at  $A_1 = [-76.663, 0, -50]$  m. The attachment points and anchor placements of cables 2, 3 and 4 are obtained from rotating  $P_1$  and  $A_1$  about the  $z$ -axis with  $90, 180,$  and  $270^\circ$  respectively. The horizontal span of each mooring cable was thus 74.8 m. As in Section 6.4, the material model of the cable was bilinear and follows eq. (55).

Results from a 100 s simulation of a regular wave with a  $T = 5$  s period time and a  $H = 0.976$  m wave height is presented in Fig. 7. The wave direction is aligned with the  $x$ -axis, propagating in the positive direction. Fig. 7(b) shows how the largest forces are found in cable 1, the sea-ward cable, as a result of the larger  $z$ -displacements of the end point position, see Fig. 7(d). This behaviour is explained by the superposition of the pitch and heave motions, being constructive for cable 1, destructive for cable 3, and essentially decoupled for cable 2 and 4.

We also notice high-frequency oscillations in the tension force. This type of oscillations have a direct implication on the fatigue life estimate of the cable, as it has a significant effect on the number of load cycles, Yang et al. (2016). In this case, they are due to the cable interference with

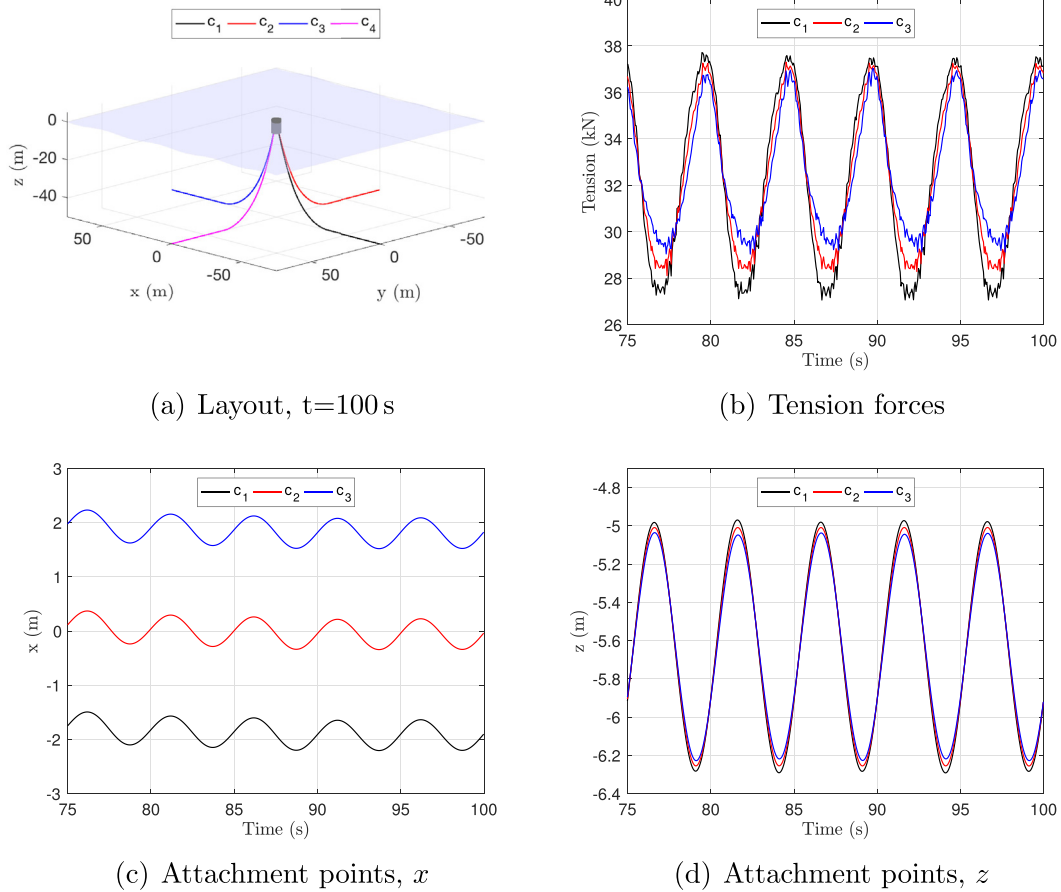


Fig. 7. Results of coupled simulations. (a): Three-dimensional view of layout at  $t = 100$  s (b)–(d): Time histories in the last 25 s of simulation for: (b) tension force, (c) attachment point  $x$ -coordinate, and (d) attachment point  $z$ -coordinate.  $c_i$  is cable  $i$  for  $i \in \{1, 2, 3, 4\}$ .

Table 5

Physical properties and computational settings used to simulate the wave energy converter (WEC) in the coupled simulation. Physical properties are adopted from Fitzgerald (2009).  $h_{wec}$  corresponds to the draft at the unmoored equilibrium position, from which the total mass can be computed.

Label	Value	Unit	Description
$d_{wec}$	5	m	diameter of WEC
$H_{wec}$	7.5	m	total WEC height
$h_{wec}$	5	m	draft of WEC
$I_{wec}^{(1)}$	1.24 E6	kg m <sup>2</sup>	moment of inertia (roll, pitch)
$I_{wec}^{(2)}$	0.47 E6	kg m <sup>2</sup>	moment of inertia (yaw)
$\rho_w$	1025	kg/m <sup>3</sup>	density of water
$\Delta t_{wec}$	0.05	s	time step size in coupling
$\tau_{wec}$	50	s	impulse response function cut off time

the ground. The results are therefore dependent on the local sea-bed properties, and how they are modelled. This simulation was made with a soft and highly dissipative ground model, to simulate sand-bottom conditions. Less dissipative sea-beds may give rise to larger tension response. We conclude that the effects of the ground and how it is modelled are large for this simulation, and that further validation studies on ground model implications are needed to separate numerical and physical effects on the cable tension history.

The mooring response is in this case smooth, and the simulation is made with a  $N = 10$  element mesh with  $p$ -adaptive elements. The elements were limited to a maximum of  $p = 8$ .

### 7. Concluding remarks

We have presented a conservative  $hp$ -adaptive DG method for the

Table 6

Physical properties and computational settings used to simulate the moorings in the coupled simulation. Physical properties are adopted from Fitzgerald and Bergdahl (2008).

Label	Value	Unit	Description
$\gamma_0$	61	kg/m	mass per meter
$d_c$	0.05	m	link diameter
$L_c$	100	m	cable length
$K_c$	100	MN	axial cable stiffness
$C_{Mt}$	0	–	tangential added mass.
$C_{Mn}$	3.8	–	normal added mass
$C_{Dt}$	0.5	–	tangential drag
$C_{Dn}$	2.5	–	normal drag
$z_G$	-50	m	vertical coordinate of ground
$K_G$	3	kPa/m	ground stiffness
$\xi_G$	10	–	ground damping
$\mu$	1.0	–	ground friction coeff.
$v_\mu$	0.01	m/s	friction velocity for the ground
$\Delta t$	0.45CFL	s	adapting time step size
$N$	10	–	number of elements per cable
$p$	1-8	–	$p$ -adaptive simulation

dynamics of mooring cables with negligible bending stiffness. As the finite element space is discontinuous and the formulation is in conservative form, the numerical model provides the necessary prerequisites for correct snap-load propagation. In smooth regions, exponential  $p + 1/2$  convergence was verified, see Fig. 1, and few elements of high-order can provide accurate and computationally efficient solutions. An  $hp$ -adaptive control algorithm with shock identification was implemented to decrease the element size  $h$  and revert to linear slope-limited elements locally around identified shocks, while retaining a high polynomial order in smoother regions. The scheme was showed to be both

accurate and computationally effective for idealised cases, see Fig. 3. Further, the conservative formulation also shows the correct shock propagation speed and shock reflection coefficients for a nonlinear material, as shown in Fig. 4. Very good agreement with experimental data, including snap loads (Fig. 5) was also achieved. Finally, to demonstrate a practical application, the software was used in coupled mode to simulate the motion of a moored wave energy converter.

Correct snap load modelling is not only important to get the maximum load in a cable for ultimate limit state design (ULS). Fatigue limit state (FLS) is also very much affected as it is estimated from the tension force history. This is clearly seen in Fig. 5(a) and (b), where the number of load cycles in the tension time history are noticeably higher in 5(a) due to the propagation of the snap load. Note also that each snap can be responsible for several load cycles due to repeated reflections in the cable. Therefore, it is not only the initial snap amplitude that is important to capture, but also the propagation of the tension shock.

In this paper, we have computed the dynamic response of mooring chains of catenary shape in both model scale and full scale. This is the traditional soft mooring solution and is the most widely used mooring concept. We see that the influence of the sea floor has an impact on the solution, introducing high-frequency content in the tension force time history. As high-frequency load cycles are introduced, the FLS design of the cables is affected. Further work and in-depth validation of ground-modelling is needed to separate physical ground-interaction effects from numerical noise generated from the touch-down region discontinuity. The numerical model presented in this paper provides a platform for further analysis of the implications of numerical modelling choices with regard to both ULS and FLS design of mooring cables subjected to snap loads.

## Acknowledgement

This work has been financed by the Swedish Energy Agency under grant numbers P40428-1 and P42246-1.

## References

- Aamo, O., Fossen, T., 2000. Finite element modelling of mooring lines. *Math. Comp. Sim.* 53, 415–422.
- Ablow, C., Schechter, S., 1983. Numerical simulation of undersea cable dynamics. *Ocean. Eng.* 10 (6), 443–457.
- ANSYS Inc, 2013. AQWA Theory Manual 15.0.
- Babart, A., Delhommeau, G., 2015. Theoretical and numerical aspects of the open source BEM solver NEMOH. In: Proc. 11th European Wave and Tidal Energy Conference, Nantes, France.
- Barter, G., Darmofal, D., 2010. Shock capturing with PDE-based artificial viscosity for DGEM: Part I. Formulation. *J. Comp. Phys.* 229, 1810–1827.
- Bauduin, C., Boulard, R., Caille, F., Newport, A., 2015. Disconnectable mooring systems for arctic conditions. In: Proc. Offshore Technology Conference, Houston, Texas.
- Bergdahl, L., Palm, J., Eskilsson, C., Lindahl, J., Dynamically scaled model experiment of a mooring cable. *J. Mar. Sci. Technol.* 4(5).
- Berger, M., Colella, P., 1989. Local adaptive mesh refinement for shock hydrodynamics. *J. Comput. Phys.* 82, 64–84.
- Bernard, P., 2008. Discontinuous Galerkin Methods for Geophysical Flow Modeling (Ph.D. thesis). Ecole polytechnique de Louvain.
- Bey, K., Oden, T., Patra, A., 1996. A parallel hp-adaptive discontinuous Galerkin method for hyperbolic conservation laws. *Appl. Numer. Math.* 20, 321–336.
- Brown, D., Mavrakos, S., 1999. Comparative study on mooring line dynamic loading. *Mar. Struct.* 12, 131–151.
- Buckham, B., Driscoll, F., Nahon, M., 2004. Development of a finite element cable model for use in low-tension dynamics simulations. *J. Appl. Mech.* 71, 476–485.
- Cockburn, B., Shu, C., 2001. Runge-Kutta discontinuous Galerkin methods for convection-dominated problems. *J. Sci. Comp.* 16, 173–261.
- Dhanak, M., Nikolaos, X., 2016. Handbook on Ocean Engineering. Springer verlag.
- DNV GL, 2014. SESAM Theory Manual for DeepC 3.0.
- Eskilsson, C., 2011. An hp-adaptive discontinuous Galerkin method for shallow water flows. *Int. J. Numer. Methods Fluids* 67, 1605–1623.
- Fitzgerald, J., 2009. Position Mooring of Wave Energy Converters (Ph.D. thesis). Chalmers University of Technology.
- Fitzgerald, J., Bergdahl, L., 2008. Including moorings in the assessment of a generic offshore wave energy converter: a frequency domain approach. *Mar. Struct.* 21, 23–46.
- Fylling, I., Wold, T., 1979. Cable dynamics - Comparison of Experimental and Analytical Results. The Ship Research Institute of Norway.
- Gobat, J., 2000. The Dynamics of Geometrically Compliant Mooring Systems (Ph.D. thesis). Massachusetts Institute of Technology and Woods Hole Oceanographic Institution.
- Gobat, J., Grosenbaugh, M., 2001. Dynamics in the touchdown region of catenary moorings. In: Proc. 11th International Offshore and Polar Engineering Conference, Stavanger, Norway.
- Godunov, S., 1959. Finite difference methods for the computation of discontinuous solutions of the equations of fluid dynamics. *Mat. Sb.* 47, 271–306.
- Greiner, W., 2003. Classical Mechanics: Systems of Particles and Hamiltonian Dynamics. Springer.
- Hann, M., Greaves, D., Raby, A., 2015. Snatch loading of a single taut moored floating wave energy converter due to focussed wave groups. *Ocean. Eng.* 96, 258–271.
- Harnois, V., 2014. Analysis of Highly Dynamic Mooring Systems: Peak Mooring Loads in Realistic Sea Conditions (Ph.D. thesis). University of Exeter.
- Hennessey, C., Pearson, N., Plaut, R., 2005. Experimental snap loading of synthetic ropes. *Shock Vib.* 12, 163–175.
- Hou, T., Le Floch, P., Why Nonconservative Schemes Converge to Wrong Solutions: Error Analysis, *Mathematics of Computation.*
- Huang, S., 1994. Analysis of three-dimensional cable dynamics. *Ocean. Eng.* 21 (6), 587–605.
- Johanning, L., Smith, G., Wolfram, J., 2007. Measurements of static and dynamic mooring line damping and their importance for floating WEC devices. *Ocean. Eng.* 34, 1918–1934.
- Karniadakis, G.E., Sherwin, S., 2003. Spectral/hp Element Methods for CFD, 2nd Edition. Oxford University Press, New York, Oxford.
- Krivodonova, L., 2007. Limiters for high-order discontinuous Galerkin methods. *J. Comp. Phys.* 226, 879–896.
- Krivodonova, L., Xin, J., Remacle, J.-F., Chevaugne, N., Flaherty, J., 2004. Shock detection and limiting with discontinuous Galerkin methods for hyperbolic conservation laws. *J. Appl. Num. Math.* 48, 323–338.
- Lax, P.D., Wendroff, B., 1960. Systems of conservation laws. *Comm. Pure Appl. Math.* 13, 217–237.
- Lindahl, J., 1984. Implicit numerisk lösning av rörelseekvationerna för en förankringskabel. Tech. Rep. Report Series A:11. Chalmers University of Technology.
- Mavrakos, S., Papazoglou, V., Triantafyllou, M., Hatjigeorgiou, J., 1996. Deep water mooring dynamics. *Mar. Struct.* 9, 181–209.
- Montano, A., Reselli, M., Sacco, R., 2007. Numerical simulation of tethered buoy dynamics using mixed finite elements. *Comp. Meth. Appl. Mech. Eng.* 196, 4117–4129.
- Morison, J., O'Brien, M., Johnson, J., Schaaf, S., 1950. The force exerted by surface waves on piles. *Pet. Trans. Amer. Inst. Min. Eng.* 186, 149–154.
- NREL and Sandia Corp, 2015. WEC-SIM Homepage. Available. <http://wec-sim.github.io/WEC-Sim>.
- Orcina Inc, 2012. OrcaFlex Manual – Version 9.5a.
- Palm, J., Paredes, G., Eskilsson, C., Taveira-Pinto, F., Bergdahl, L., 2013. Simulation of mooring cable dynamics using a discontinuous Galerkin method. In: Proc. 5th International Conference on Computational Methods in Marine Engineering, Hamburg, Germany.
- Palm, J., Eskilsson, C., Paredes, G., Bergdahl, L., 2016. Coupled mooring analysis for floating wave energy converters using CFD: formulation and validation. *Int. J. Mar. Eng.* 16, 83–99.
- Persson, P., Peraire, J., 2006. Sub-cell shock capturing for discontinuous Galerkin methods. In: Proc. 44th AIAA Aerospace Sciences Meeting and Exhibit.
- Safetec, 2013. Causal Relationships and Measures Associated with Structural and Maritime Incidents on the Norwegian Continental Shelf. Tech. Rep., Petroleum Safety Authority, Norway.
- Savin, A., Svensson, O., Leijon, M., 2012. Azimuth-inclination angles and snatch load on a tight mooring system. *Ocean. Eng.* 40, 40–49.
- Shin, H., 1991. Analysis of extreme tensions in a snapping cable. In: Proc. 1st International Offshore and Polar Engineering Conference, Edinburgh, United Kingdom.
- Spak, K., Agnes, G., Inman, D., Cable modeling and internal damping developments, *Appl. Mech. Rev.* ASME 65(1).
- Sweby, P., 1984. High resolution schemes using flux limiters for hyperbolic conservation laws. *SIAM J. Numer. Anal.* 21 (5), 995–1011.
- Thies, P., Johanning, L., Smith, G., 2012. Lifecycle fatigue load spectrum estimation for mooring lines of a floating marine energy converter. In: Proc. 31st International Conference on Ocean, Offshore and Arctic Engineering, Rio de Janeiro, Brazil.
- Tjavaras, A., 1996. The Dynamics of Highly Extensible Cables (Ph.D. thesis). Massachusetts Institute of Technology.
- Toro, E., 2001. Shock-capturing Methods for Free-surface Shallow Flows. Wiley and Sons, Ltd.
- Triantafyllou, M., Bliet, A., Shin, H., 1985. Dynamic analysis as a tool for open-sea mooring system design. *SNAME Trans.* 93, 302–324.
- Vassalos, D., Kourouklis, A., 1998. Experimental, Theoretical and Full-scale Investigation on the Snap Loading of Marine Cables. Main report OTH 558. University of Strathclyde. ISBN: 0-7176-1595-2.
- Walton, T., Polachek, H., 1959. Calculation of transient motion of submerged cables. *Math. Comp.* 14, 27–46.
- Yang, S., Ringsberg, J., Johnson, E., Hu, Z., Palm, J., 2016. A comparison of coupled and de-coupled simulation procedures for the fatigue analysis of wave energy converter mooring lines. *Ocean. Eng.* 117, 332–345.